Materials Science & Engineering C 108 (2020) 110404

Contents lists available at ScienceDirect

Materials Science & Engineering C

journal homepage: www.elsevier.com/locate/msec

Synthetic open cell foams versus a healthy human vertebra: Anisotropy, fluid flow and μ-CT structural studies

Sergio Gómez González[a], José Fernando Valera Jiménez[a], Gerard Cabestany Bastida[a], Maria Daniela Vlad[b,c], José López López[a], Enrique Fernández Aguado[a,*]

[a] Research Group of Interacting Surfaces in Bioengineering and Materials Science (InSup), Technical University of Catalonia (UPC), Avda. Diagonal 647, 08028 Barcelona, Spain
[b] Faculty of Medical Bioengineering, "Grigore T. Popa" University of Medicine and Pharmacy Iasi, Str. Kogălniceanu 9-13, 700454 Iasi, Romania
[c] TRANSCEND Research Centre, Regional Institute of Oncology, Str. G-ral Henri Mathias Berthelot 2-4, 700483 Iași, Romania

ARTICLE INFO

Keywords:
Trabecular vertebral bone
Synthetic bone-like foams
Bone histomorphometric indices
Permeability
Micro-computed tomography
Computational fluid dynamics

ABSTRACT

Commercial synthetic open-cell foams are an alternative to human cadaveric bone to simulate in vitro different scenarios of bone infiltration properties. Unfortunately, these artificial foams do not reproduce the anisotropic microstructure of natural bone and, consequently, their suitability in these studies is highly questionable. In order to achieve scaffolds that successfully mimic human bone, microstructural studies of both natural porous media and current synthetic approaches are necessary at different length scales. In this line, the present research was conducted to improve the understanding of local anisotropy in natural vertebral bone and synthetic bone-like porous foams. To attain this objective, small volumes of interest within these materials were reconstructed via micro-computed tomography. The anisotropy of the microstructures was analysed by means of both their main local histomorphometric features and the behaviour of an internal flow computed via computational fluid dynamics. The results showed that the information obtained from each of the micro-volumes of interest could be scaled up to understand not only the macroscopic averaged isotropic and/or anisotropic behaviour of the samples studied, but also to improve the design of macroscopic porous implants better fitting specific local histomorphometric scenarios. The results also clarify the discrepancies in the permeability obtained in the different micro-volumes of interest analysed.

Statement of significance: A deep insight comparative study between the porous microstructure of healthy vertebral bone and that of synthetic bone-like open-cell rigid foams used in in vitro permeability studies of bone cement has been performed. The results obtained are of fundamental relevance to computational studies because, in order to achieve convergence values, the computation process should be limited to small computation domains or micro-volumes of interest. This makes the results specific spatial dependent and for this reason computation studies cannot directly capture the macroscopic average behaviour of an anisotropic porous structure such as the one observed in natural bones. The results derived from this study are also important because we have been able to show that the specific spatial information contained in only one healthy vertebra is enough to capture, from a geometric point of view, the same information of "specific surface area vs. porosity" – in other words, the same basic law – that can also be found in other human bones for different patients, even at different biological ages. This is an important finding that, despite the efforts made and the controversies formulated by other authors, should be studied more thoroughly with other bone species and tissues (healthy and/or diseased). Moreover, our results should help to understand that, with the extensive capabilities of current 3D printing technologies, there is an enormous potential in the design of biomimetic porous bone-like scaffolds for bone tissue engineering applications.

* Corresponding author at: Department of Materials Science and Metallurgical Engineering, Technical University of Catalonia (UPC), Avda. Diagonal 647, 08028 Barcelona, Spain.
E-mail address: enrique.fernandez@upc.edu (E. Fernández Aguado).

https://doi.org/10.1016/j.msec.2019.110404
Received 2 September 2019; Received in revised form 22 October 2019; Accepted 6 November 2019
Available online 06 November 2019
0928-4931/

1. Introduction

Nowadays, due to the ageing of modern society, there are many clinical problems associated with degenerative bone diseases that need to be solved [1,2]. In this scenario, the osteoporosis induced vertebral compression fractures are becoming more frequent as life expectancy increases [3]. In response to this situation, percutaneous vertebroplasty and kyphoplasty are minimally invasive surgery procedures used to stabilise the weakened vertebra and, when necessary, to improve the fixation of cement-augmented pedicle screws in the spinal region [4–7]. However, some clinical studies have pointed out that bone cement does not homogeneously infiltrate in the vertebral bone, leading to preferential flow and leakage in some instances [8]. Thus, some authors have focused their research interest on the measurement of average macroscopic permeability properties exclusively associated with the average porous structure of natural vertebral bone [9–13]. Others, in order to overcome the scarce availability of bone tissue samples, used synthetic isotropic open-cell foams to carry out bone cement infiltration tests on the assumption that these foams have both similar microarchitecture and mechanical behaviour to those of natural bone [14–20]. In this sense, the literature includes studies evaluating ceramic foams [21,22], open-cell metal foams [23,24] or glass foams [25]. Additionally, some authors have computed the permeability of virtual macro-porous models by means of numerical methods with the aim of assessing the anisotropic behaviour of trabecular bone at low length scale [26,27]. In a similar approach, other computational studies have established certain correlations between the average permeability and some average histomorphometric parameters (both at the macroscopic length scale) of porous bone samples [13,26,28–31]. Computational fluid dynamics (CFD) studies have showed that permeability of trabecular vertebral bone can be correlated to the bone volume to total volume ratio (BV/TV), the bone surface to total volume ratio (BS/TV), the trabecular number (Tb.N), the structural model index (SMI), the trabecular separation (Tb.Sp) and the degree of anisotropy (DA) [28,29]. Moreover, some works have highlighted that bone anisotropy is, at the low length scale, the microstructural feature that most influences the fluid behaviour inside the material [9,29]; not in vain, the orientation of trabeculae in the stress direction promotes preferential fluid flow [32]. For this reason, the reported average permeability values at macroscopic length scale, measured at different locations, vary in more than six orders of magnitude [9,12,13,27,29].

In this scenario, research is necessary to develop reliable predictive models linking the macroscopic fluid flow properties of bone-like materials to their exact internal microstructure. These studies should help to understand not only bone cement infiltration issues but also body fluid transport of minerals and nutrients. Additionally, such studies could contribute to manufacturing, by means of three dimensional (3D) printing technologies, authentic biomimetic bone-like porous scaffolds able to interact with the surrounding body fluids in a more similar manner as replaced or neighbouring bone do [33].

Despite the numerous investigations carried out with both synthetic artificial models and real vertebra, very few studies have compared, at the same scale, the exact geometric and histomorphometric characteristics of commercial synthetic foams and natural bone and, not least, the effect that these differences have on their infiltration. On that basis, the present investigation finds its own meaning. Since the study was based on computational methods, its objective was not to evaluate macroscopic bone infiltration properties for surgery applications at all. Today, such ambitious studies would not be possible to compute with the level of detail required for accurate results. Rather, our interest was related to the microscopic structural anisotropy of two representative commercial bone-like foams and one representative human vertebra, with special attention being paid to the effect of the microstructural features on certain local flow properties. The assessment of small volumes of interest within the porous materials represents a strategy to meet the abovementioned targets without the need of excessive computing times. Thus, the use of the same experimental approach (i.e. computation experiments under the same boundary conditions) should determine, with the help of image analysis and CFD software, whether synthetic foams could reproduce the microscopic behaviour of certain flow properties inside bone under in vitro conditions. This perspective should also provide clarification about the scalability of specific local properties of the porous media towards the macroscopic averaged behaviour of bigger samples.

2. Materials and methods

2.1. μCT scan of selected samples

To achieve the objective proposed in the previous section, two representative commercial synthetic foams (*Sawbones©, Inc., Vashon Island, USA*), with porous structures similar to those of cancellous bone, and one healthy third lumbar spine vertebra (L3) were selected. The open-cell foams are provided as an alternative to human cadaveric bone for orthopaedic devices, biomechanical testing and in vitro studies of vertebral cement augmentation procedures. Some minor details about their properties can be found in their commercial catalogues (Ref.: 1522-505 and -507). Fortunately, an independent and comprehensive study focussing on the chemical, physical and histomorphometric properties of these same open-cell rigid foams can be found in the literature [20]. In the present study, the foams (fiber-glass (46(± 12) vol%) reinforced polyurethane [20]) were coded according to their commercial colour, white foam (WF; Ref. 1522-505) and blue foam (BF; Ref. 1522-507). The foams were μCT-scanned (eXplore Locus, GE Healthcare; 80 kVp, 0.5 mA; recorded volume = $30 \times 30 \times 25\,mm^3$; voxel size = $0.046 \times 0.046 \times 0.046\,mm^3$; 12 s per image) leading to a total number of 535 image slices. On the other hand, the representative L3 human vertebra, coded as ESA was an open source file of a healthy lumbar cadaver vertebra (which unfortunately is currently unavailable at its original link: http://bone3d.zib.de/data/2005/ESA29-99-L3/) containing a μCT vertebral body data set of 970 image slices (Scanco μCT 80, SCANCO Medical; 50–70 kVp, 0.16 mA; recorded volume = $76 \times 76 \times 36\,mm^3$; voxel size = $0.0371 \times 0.0371 \times 0.0370\,mm^3$; 12 s per image) obtained by the European Space Agency (ESA) and offered as an open access file to the scientific community [34]. Although the European Space Agency did not report the gender and age of this representative L3 vertebra, this information is irrelevant for the objectives of the present study, which in turn, was aimed at mapping the internal microstructure of this specific vertebra at ten different representative spatial locations, hereinafter referred as micro-volumes-of-interest (micro-VOIs). It is within this approach that the information obtained at local level from such specific micro-VOIs could even represent, if scaled up, different average gender and age situations. Thus, these micro-VOIs were randomly selected in order to take into consideration the local anisotropy of the samples.

In order to make things clear, the Fig. 1.a–c show the experimental set-up followed to obtain the virtual structural models of the different micro-VOIs. First, an appropriate μCT image stack, in DICOM format, was selected (Fig. 1.a). Then, the images were exported to the image processing software *ScanIP©* (*Simpleware© Ltd, Exeter, UK*) for noise reduction, smoothing, segmentation with automated tools (Fig. 1.b) and 3D virtual reconstruction (Fig. 1.c). The Tb.Th and Tb.Sp indices were obtained with *BoneJ* [35], an *ImageJ* [36] plugin. Here the procedure involved the analysis of 10 subsets of 50 consecutive μCT-images for each of the three samples studied. The Tb.Th and Tb.Sp indices associated with each subset were estimated and used to calculate the same average indices referring to the entire macroscopic samples. Additionally, the BS/TV and BV/TV indices of the different micro-VOIs reconstructed (foams: $4 \times 4 \times 4\,mm^3$; L3 vertebra: $5 \times 5 \times 5\,mm^3$) were calculated with the help of *Rhinoceros3D©* (*Robert McNeell & Associates*).

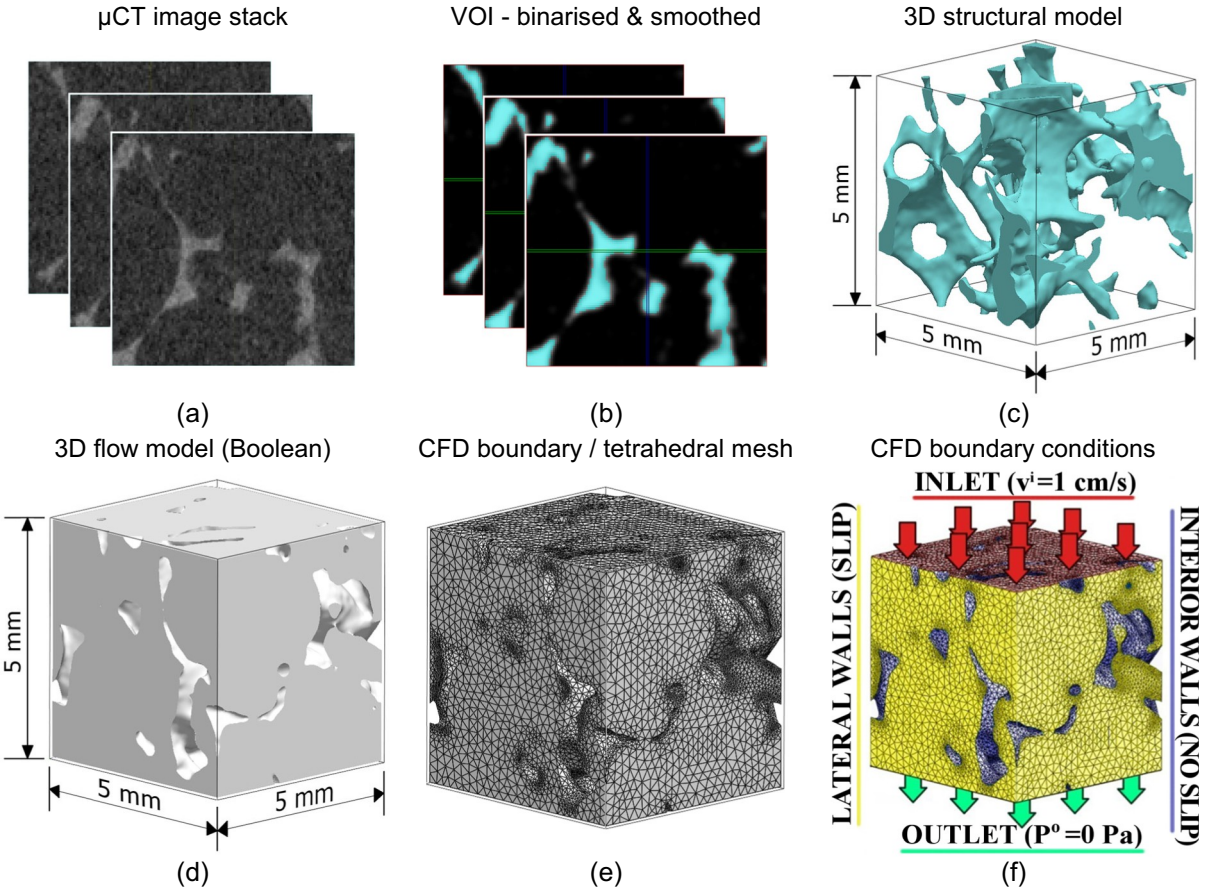

Fig. 1. Experimental process followed to obtain the structural and the CFD models. a) Selection of the adequate μCT image stack; b) Binarisation and smoothing of the micro-VOIs selected; c) 3D virtual reconstruction of the structural model; d) Boolean operation applied to the structural model to obtain the 3D CFD model; e) Meshing process of the CFD model; and f) Application of boundary conditions to the CFD model to compute its fluid dynamic properties.

2.2. Fluid computation of virtual models

Once the structural models were obtained, a Boolean operation was applied to generate the inverted models used to compute the CFD simulations (Fig. 1.d). Then, the inverted models were meshed with tetrahedral elements by using the software *ScanFE©* (*Simpleware© Ltd, Exeter, UK*) and its +FE-Free meshing algorithm (Fig. 1.e). Convergence results and suitable computing times were attained with 0.8 million tetrahedral elements, on average, by using an HP Z800 Workstation with Intel© Core i5 and 96 GB of RAM. Once convergence was ensured, the optimum meshed models, shown in Fig. 1.e (*ScanIP©*), were exported to *Comsol Multiphysics©* (*Comsol©, Inc., Burlington, USA*), version 4.3, and appropriate boundary conditions were applied in order to compute the fluid properties (Fig. 1.f). These were based on Navier-Stokes equations under laminar and stationary flow because under these conditions each porous micro-VOI can be easily computed to highlight its local material properties. Additionally, fluid computation was carried out along the 3 symmetry axes of each cubic micro-VOI with the challenge of taking into consideration its intrinsic anisotropy.

The boundary conditions (Fig. 1.f) were set as follows; first, an axis-flow direction was selected (x, y and/or z; right-handed orthogonal reference system); then, one of the VOI-faces perpendicular to such axis was set as the flow inlet, with an inlet velocity $v^i = 1$ cm/s; similarly, the opposite face was set as the outlet boundary, with an outlet pressure $P^o = 0$ Pa; then, the wall interfaces were defined as no-slip faces, whereas the slip boundary condition was set for the remaining lateral VOI-faces. The inlet velocity was set as $v^i = 1$ cm/s because this was the average fluid flow velocity measured at the end of a standard vertebroplasty cannula when this was being infiltrated with bone cement at fluid flow rate of 5.5 cm^3/min [37]. This flow rate is a common value in vertebroplasty procedures. Moreover, the following physical properties were selected for the fluid: dynamic viscosity, $\eta = 2$ kPa·s (similar to that of low viscosity acrylic cements [38]) and density, $\rho = 2.2$ g/cm^3 (same order of that reported for calcium phosphate cements [39]). These values were taken from the literature to better approach Newtonian flow conditions, which are easier to compute. However, since we were doing the computations of the different porous micro-VOIs under the same experimental conditions, it should be noted that the use of a particular value for the viscosity of the fluid was not a relevant issue.

The fluid properties computed for each micro-VOI were the pressure drop ($P^{i\text{-}o}$[Pa]), the flow-velocity (V^o[m/s]), the shear rate (γ[1/s]) and the vorticity (ω[1/s]). Moreover, the values of the pressure drop were collected to determine the intrinsic permeability of each micro-VOI by Darcy's law [13,40,41].

Additionally, the tortuosity associated with each sample was evaluated by means of 2D CFD simulations based on boundary conditions similar to those explained above. To this end, once the fluid field was computed in models with a size of approximately 30 × 30 mm^2 (dimensions which are larger than those mentioned for the 3D computations), the Particle Tracing Module of *Comsol Multiphysics©* was applied to calculate the routes followed by particles in the different macro-VOIs. For simplicity, more details of these concrete calculations have been included in the Results and discussion section with the aim of favouring a better understanding of them.

3. Results and discussion

First of all, Fig. 2 shows some examples of 3D virtual μCT structural

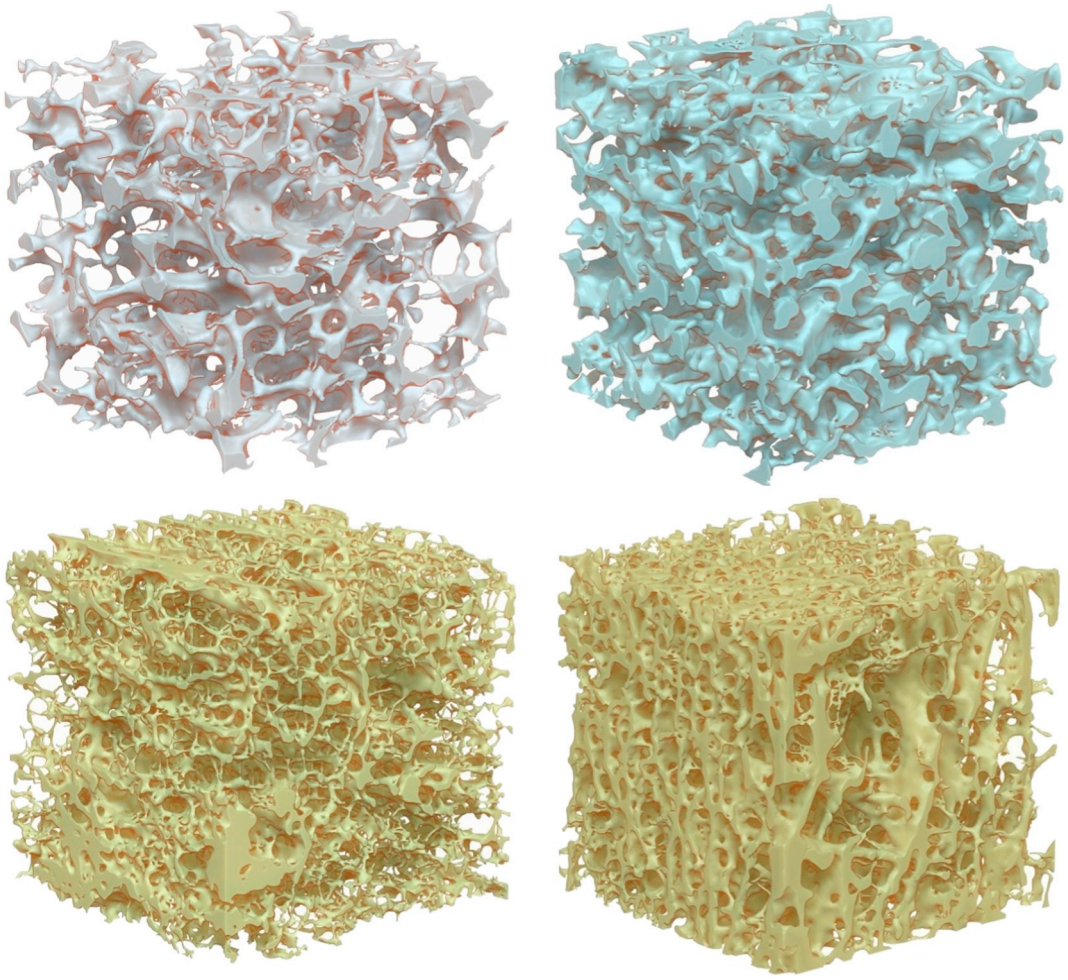

Fig. 2. 3D virtual μCT reconstructions of cubic macro-VOIs with a size of 15 × 15 × 15 mm^3 for the samples analysed: top left (in white colour): White Foam (WF); top right (in blue colour): Blue Foam (BF); down left and down right (in yellow colour): central and peripheral area, respectively, of lumbar vertebra ESA (Ref. [34]). (For interpretation of the references to colour in this figure legend, the reader is referred to the web version of this article.)

models reconstructed from the porous samples studied. The macro-VOIs shown in this figure, with dimensions of 15 × 15 × 15 mm^3, were only generated to qualitatively highlight the different microstructural trabecular features in the samples at macroscopic scale. The pictures clearly show that, on average, WF (top left in white colour) is more porous than BF (top right in blue colour), and the latter is more porous than vertebra ESA (down in yellow colour). The pictures also show that, on average, both WF and BF are isotropic with mainly rod-like units and minor contribution of plate-like units. On the other hand, the vertebra ESA revealed isotropic rod-like nature in its central region (down left; typical of spongious bone) and anisotropic plate-like character (longitudinal in the main stress orientation) in its periphery (down right; typical of compact bone). These pictures also help visualise some expected tendencies for several important histomorphometric indices. For example, on average, Tb.N, BV/TV and BS/TV will follow the order of WF < BF < ESA; in contrast, Tb.Sp will follow the one of WF > BF > ESA. These tendencies can be used to predict that, under equal boundary conditions, the macroscopic permeability of the samples should follow, on average, the order of WF > BF > ESA.

Similarly, Fig. 3 shows a collection of 3D virtual μCT structural models reconstructed from 5 arbitrary locations in the macroscopic VOIs (Fig. 2) corresponding to the foams. However, in this case, the size of the micro-VOIs selected was 5 × 5 × 5 mm^3, that is a fraction of 1/27 of the macro-VOIs represented in Fig. 2 (i.e. 15 × 15 × 15 mm^3). The intention of this downscaling study was to clarify whether the macroscopic isotropy observed in Fig. 2 in both, the WF and the BF, can be represented by a scalable model in a bottom-up approach. To that end, Fig. 3 shows, as an example, 3 of the 5 virtual structural models reconstructed from each of the foams, in order of increasing BV/TV ratio (from left to right). It is important to mention that the complete series of numerical data was BV/TV(%) = 5.39; 6.62; 7.16; 7.27; and 7.45 (i.e. an average value of < BV/TV(%) > = 6.8(± 0.8); (± StD; standard deviation)) for the WF, and BV/TV(%) = 9.76; 10.01; 10.60; 10.74; and 10.83 for the BF (i.e. < BV/TV(%) > = 10.4(± 0.5)).

These data confirm that, on average, the BF is more compact than the WF and, at least numerically, the BF can be interpreted as an extension of the WF. This is an important remark because, on the basis of the isotropy found in both foams, it helps figure out a certain continuity in each of the possible local measurements of structure-related properties, such as local permeability (i.e. permeability related to each specific VOI), as will be discussed later.

Fig. 4 shows, in a similar way as Fig. 3, a collection of 3D virtual μCT reconstructions generated from 10 specific locations (denoted by P1, P2, etc.) of the entire vertebra ESA (see the top image in Fig. 4 to find the 10 specific locations).

In this case, the VOI intended for the analysis was reduced to 4 × 4 × 4 mm^3 due to the more intricate trabecular microstructure of the vertebra ESA in comparison with the foams, as observed in Fig. 2, which otherwise have led to time computing problems. Thus, the micro-VOIs selected were nearly 1/53 of that represented in Fig. 2 (i.e. 15 × 15 × 15 mm^3). Moreover, these micro-VOIs were distributed along the entire vertebra to precisely cope with its anisotropic character

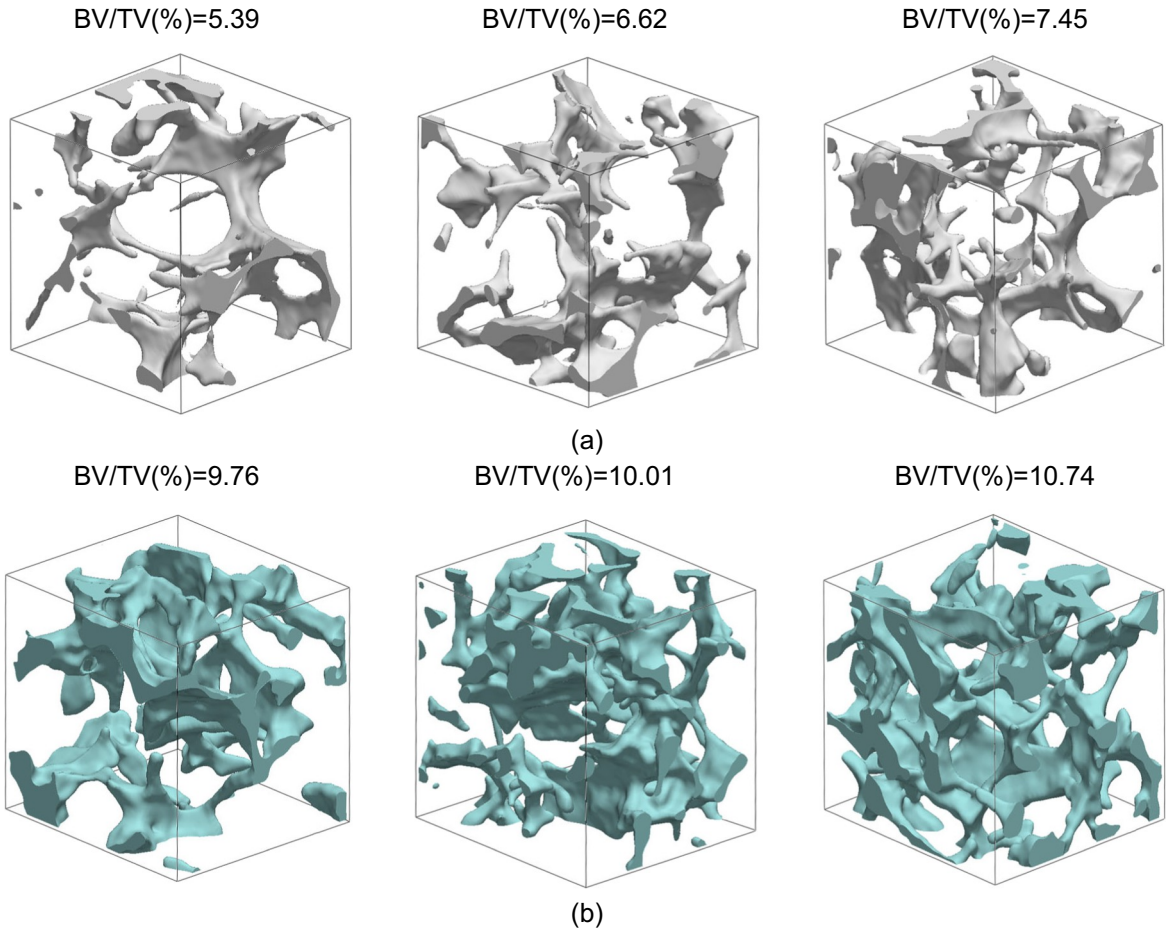

Fig. 3. A collection of 3D virtual μCT reconstructions carried out in cubic micro-VOI with a size of $5 \times 5 \times 5\,mm^3$ for both, the WF (a) and the BF (b). Note: The computed BV/TV histomorphometric index is included on the top of each virtual model.

as observed in Fig. 2 (see the down figures representing a more porous tissue (left – central area of the vertebra) versus a more compact one with a higher proportion of plate-like trabeculae (right – peripheral area of the vertebra)).

In Fig. 4, only 6 of the 10 virtual structural models corresponding to the selected specific locations have been represented. The complete series of numerical data in order of increasing values for the BV/TV(%) ratio was P2 = 7.23; P6 = 9.09; P4 = 9.25; P7 = 10.47; P9 = 14.31; P8 = 15.35; P5 = 15.79; P3 = 15.93; P1 = 17.28; and P10 = 21.98 (i.e. an average value of < BV/TV(%) > = 13.7(± 4.6)). These data confirm that, on average, at a macroscopic level (in this study this means an equivalent situation to VOI = $15 \times 15 \times 15\,mm^3$), the vertebra ESA is effectively more compact than both, the WF and the BF. However, when looking at more local scale (in this study this means VOI = $4 \times 4 \times 4\,mm^3$), data show that vertebra ESA contains specific locations that are identical to WF and BF (i.e. specific BV/TV values in the interval covered by the foams; see locations and values obtained for P2, P6, P4 and P7). This numerical agreement is also captured by the similar isotropic rod-like microstructures contained inside those particular VOIs. In this sense, the specific locations studied in the vertebra ESA act as a continuous extension of the experimental domain covered by the foams. In contrast, when focusing on the other values obtained for the BV/TV ratio, which are out of the range covered by the foams, the models associated with these values (see P5, P1 and P10) seem to be more anisotropic rather than isotropic; the microstructural features evolve from nearly an isotropic cylindrical rod-like model (P5) to a plate-like model (P10) where plates are mainly oriented longitudinally. As a result, it can also be anticipated that, despite the fact that some histomorphometric indices can capture the continuity of this domain (for example BV/TV), certain local structure-related material properties (for example permeability) should show particular tendencies depending on other histomorphometric indices more capable to capture the specific structural differences found in similar micro-VOIs. To clarify this, the following figure follows.

Fig. 5 helps clarify the differences in geometry, in absolute terms, revealed by the data collected in relation to the specific histomorphometric features of the micro-VOIs studied. The figure on the top left shows the correlation found between the absolute computed Bone-Volume (BV) and its corresponding absolute Bone-Surface (BS). The data showed linear correlation, $BS(mm^2) = a + b \cdot BV(mm^3)$, with a = 35.5(± 10.6), b = 8.7(± 1.0) and squared correlation coefficient of R^2 = 0.79962, which means that 80% of this linear correlation can be explained only by these two absolute indices (i.e. BS and BV).

This figure also shows that effectively the WF, the BF and the ESA samples represent a continuous domain from the angle of its absolute BV value (see the x-axis), as previously highlighted in Figs. 3 and 4. In fact, this figure illustrates that values of BV increase in the order of ESA < WF < BF. While WF and BF are correctly ranked (WF < BF in terms of BV; with a similar size of the micro-VOIs analysed: $5 \times 5 \times 5\,mm^3$), the data collected from ESA showed lower values for BV because the micro-VOIs in this case were also smaller (i.e. VOI = $4 \times 4 \times 4\,mm^3$). After clarifying this point, what the top left graph in Fig. 5 shows is, in fact, the absolute linear correlation found between related computed values of BS and BV: small values of BV also involve small values of BS.

However, this top left graph clarifies neither how small these values are nor how different values can be compared. To cope with this, the top right graph in Fig. 5 has been built. This new graph represents the

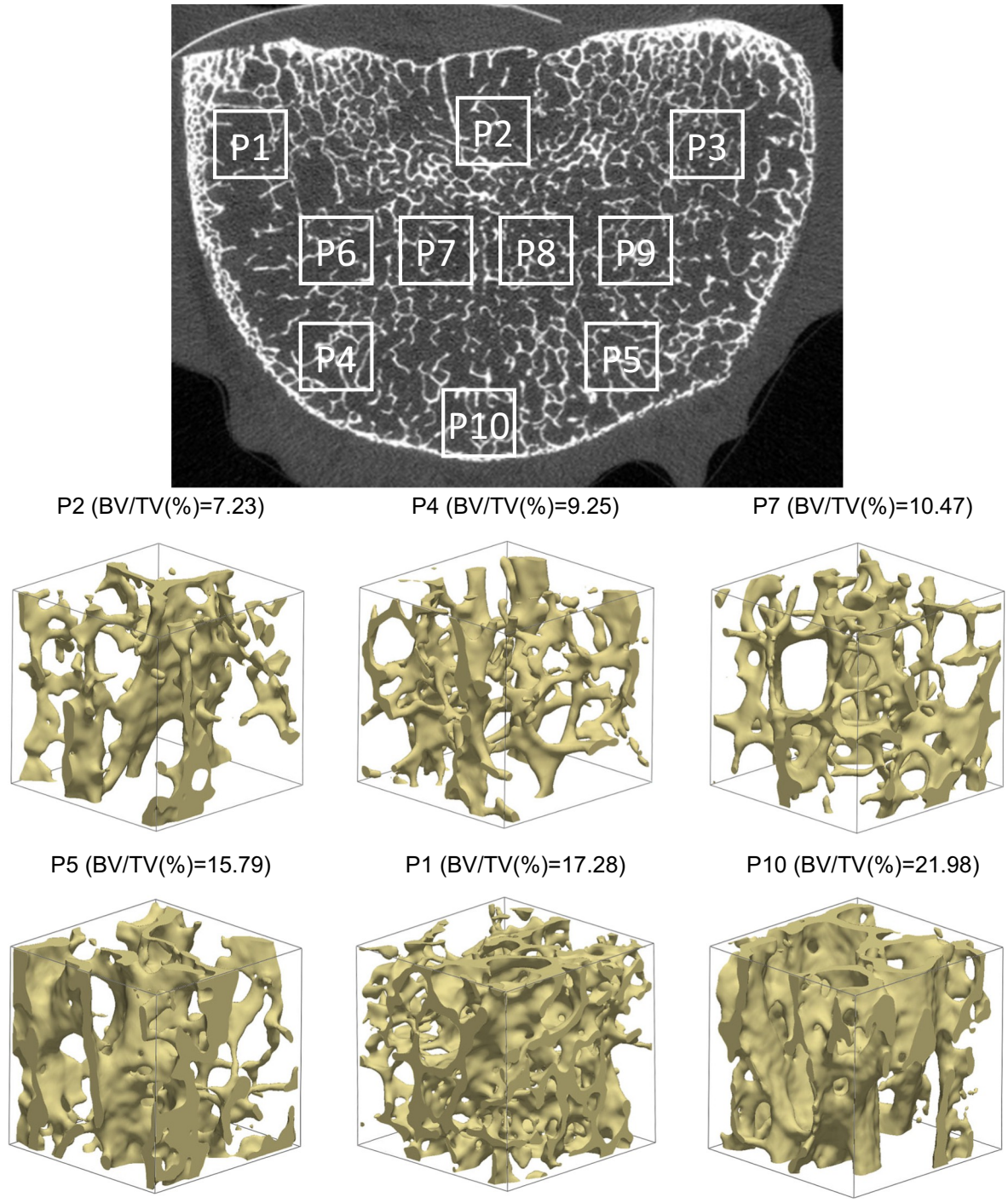

Fig. 4. A collection of 3D virtual μCT reconstructions carried out in cubic micro-VOIs with a size of $4 \times 4 \times 4\,mm^3$ for the vertebra ESA. The 10 specific locations used to build the virtual models are denoted by P_i ($i = 1,\ldots,10$) in the top picture (transversal plane of the vertebra). For clarity, only 6 reconstructions are shown, each with their computed BV/TV index on the top.

same previous data in an equivalent but more intuitive way. In the x-axis, the variable represented is the radius of an equivalent sphere (R_v) having the same volume measured for each BV data (i.e. $R_v = \left(\frac{3}{4\pi} \bullet BV\right)^{1/3}$). Then, the BS data have been represented in the y-axis and their values have been compared with the surface values of perfect spheres having an equivalent radius R_v (i.e. $BS_{sphere} = 4\pi \cdot (R_v)^2$). What is notorious of this representation is that the BS values for the data collected were properly fitted to a multiple of the BS values of a perfect sphere (i.e. $BS_{data} = K \cdot BS_{sphere}$), with $K = 5.6(\pm 0.2)$ and squared correlation coefficient of $R^2 = 0.78989$, this latter being similar to that found for the linear representation of the top left figure (see previous results, $R^2 = 0.79962$). The general conclusion is clear: all the micro-VOIs analysed for the porous samples (WF, BF and ESA) can be seen as ones containing a sphere with irregular surface, each BS value having on average 5.6 times more surface than its corresponding perfect sphere (i.e. having the same equivalent radius R_v).

To clarify even more the relative correspondence between the collected data, the bottom pictures of Fig. 5 were also built. The bottom-left graph in Fig. 5 shows the linear correlation found between the BS/BV ratio and BV (i.e. $BS/BV(mm^{-1}) = a + b \cdot BV(mm^3)$), with

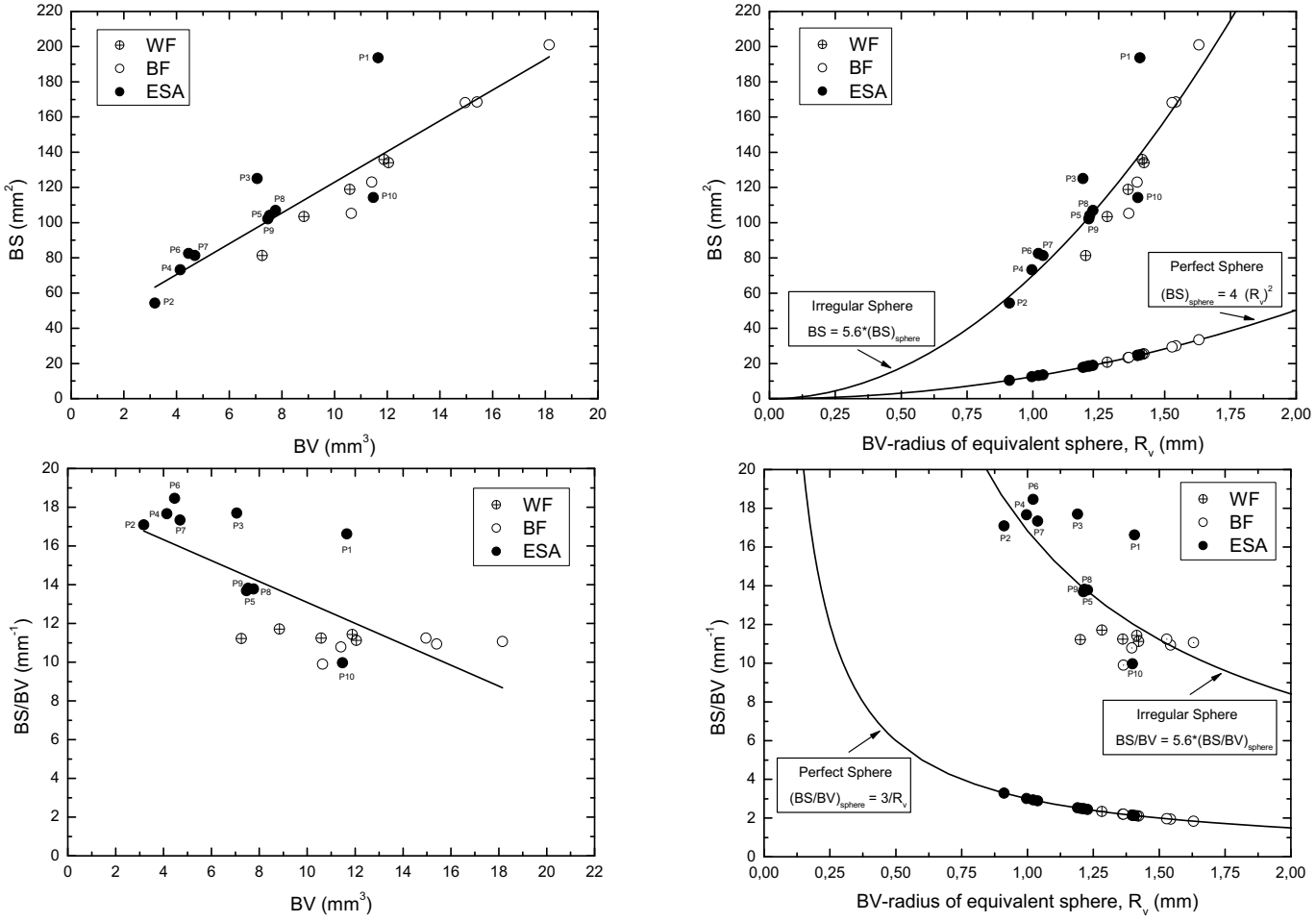

Fig. 5. On the left, interdependence between data of absolute Bone-Volume (BV), absolute Bone-Surface (BS) and relative BS/BV ratio; on the right, data interpretation according to an equivalent spherical model containing perfect and/or irregular surfaces. Note that the traceability of the virtual models of the vertebra ESA is contemplated in the figures. See the text for a detailed explanation.

$a = 18.5(\pm 1.3)$, $b = -0.54(\pm 0.12)$ and squared correlation coefficient of $R^2 = 0.52317$, which means that only 52% of this linear correlation can be explained by these two measures (i.e. BS/BV and BV).

Similarly, the bottom right figure makes a conversion of the previous data to an equivalent situation of perfect spheres versus irregular ones. In the case of a perfect sphere, it is known that $BS/BV_{sphere} = 3/R_v$. Again, this representation showed that the whole set of the data measured (the BS/BV values drawn from the trabecular models) fitted a multiple of the expected BS/BV values for perfect spheres with the same volume as that contained in their equivalent trabecular models (i.e. $BS/BV_{data} = K \cdot BS/BV_{sphere}$); with $K = 5.6(\pm 0.2)$, and squared correlation coefficient of $R^2 = 0.61119$ (i.e. better than that obtained for the linear fit).

Some conclusions can be obtained from this analysis. First, it is still valid to say that, on average, each computed data showed a BS/BV ratio that is 5.6 times higher than the one corresponding to its equivalent perfect sphere. In this sense, the picture of how irregular the surface of a like-sphere is as compared with an equivalent perfect sphere is still valid to try to cope with the relative differences found between the whole set of micro-VOIs selected for the different samples (WF, BF, and ESA). This means that, under exactly equal conditions, the vertebra ESA effectively shows a more intricate internal microstructure than that observed for both foams, which was evident from both, the BV/TV values reported in Figs. 3–4 and their corresponding 3D virtual μCT reconstructions.

Under this approach, the bottom left graft in Fig. 5 even allows a more individual and specific comparison between the data obtained. For example, just by looking at the WF and the BF data, it can be observed that 9 of the 10 small analysed VOIs showed nearly the same BS/BV value (i.e. $11.2(\pm 0.3)$ mm^{-1}) for the whole range of computed BVs (i.e. $7 < BV(mm^3) < 18$). This observation agrees perfectly with Fig. 2 and the fact that both foams were strictly isotropic, and so scalable.

On the other hand, the conclusions obtained for the vertebra ESA will clearly depend on the specific location of the micro-VOI analysed, in agreement with the general observation drawn from Fig. 2, where the anisotropy of the vertebra was evident. For example, the bottom left picture in Fig. 5 shows the same values of BS/BV ($13.8(\pm 0.05)$ mm^{-1}) and BV ($7.6(\pm 0.1)$ mm^3) for the locations P5, P8 and P9; this means that similar isotropic microstructures should be found along the vertebral zone covered by these locations (see also the virtual model of P5 reconstructed in Fig. 4). A comparison between P1 and P10 (same BV but quite different BS/BV ratio) leads to the conclusion that effectively P1 must show a more intricate internal microstructure in line with a rod-like model, while P10 should fit a more compact plate-like model microstructure (see also the virtual models of P1 and P10 in Fig. 4). Other comparisons can be made between the other points but those made here should be enough to conclude that the vertebra (human natural bone) will be more sensitive (i.e. more care must be taken in its analysis) than the foams (synthetic bone model) when computing, at low scale, structure-related material properties, for example, the permeability of those porous structures.

In the same way as Fig. 5 does, Fig. 6 helps clarify the relative differences in geometry between the selected micro-VOIs in the samples

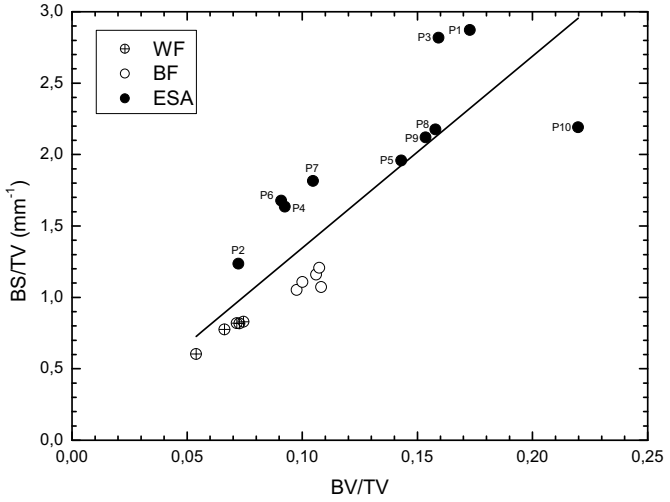

Fig. 6. Interdependence observed between the BS/TV and the BV/TV histomorphometric indices measured for the specific VOIs studied. A linear regression can explain 72% of the correlation.

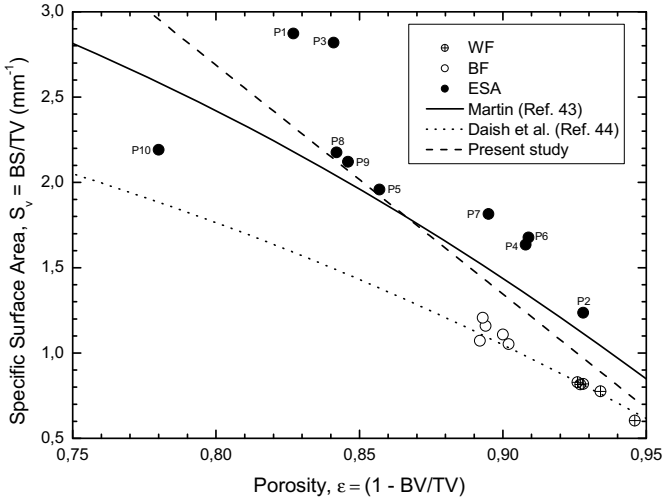

Fig. 7. Linear correlation observed between our computed specific surface area and porosity data ($S_v = a + b \cdot \epsilon$; a = 13.42(± 1.75); b = − 13.41(± 2.0); R^2 = 0.72). The 5th order polynomial regression curves proposed by Martin (Ref. [43]) and Daish et al. (Ref. [44]) are also included. See the text for details.

studied. In this case, the absolute values of BS and BV contained inside the selected micro-VOIs were normalised against the total volume (TV) of each micro-VOI. A linear regression showed that only 72% of the observed correlation (R^2 = 0.7222) was explained by a scalable model ($BS/TV = a + b \cdot (BV/TV)$; $a = 0(\pm 0.2)$; $b = 13.4(\pm 2.0)$). This clearly indicates that local differences, which are associated with different microarchitectures (rod-like, plate-like and/or mixture models), are ultimately responsible for this lack of correlation. This was in agreement with the observations made in Fig. 5 (see discussion concerning perfect spheres versus irregular ones). Fig. 6 also revealed that those micro-VOIs in ESA having values of porosity ϵ ($\epsilon = 1 - (BV/TV)$) in the same range than WF and BF (i.e. P2, P4, P6, P7) had higher values of BS/TV than the micro-VOIs in the foams. This confirms that, under equal conditions, the trabecular patterns found in ESA were more complex and intricate (and therefore implied a higher specific surface area) than the ones in the foams.

Fig. 6 also shows that, on average, most of the micro-VOIs analysed in the vertebra ESA (P5, P9, P8, P3, P1, P10) had lower porosity values than the ones in the foams. It also shows that the micro-VOIs furthest from the regression line are precisely the most compact and anisotropic ones, and so are closer to a plate-like rather than a rod-like microstructure. In general, our data showed the same linear behaviour than that obtained by Fyhrie et al. [42] in a similar range ($0.1 \leq BV/TV \leq 0.2$; R^2 = 0.84) for vertebral trabecular bone excised from the centre of different vertebrae and individuals. Furthermore, the other important observation is that our data covered, with only one representative healthy human vertebra (and 10 different micro-VOIs of $4 \times 4 \times 4\,mm^3$), the same porosity range and the same specific surface values than those obtained by Fyhrie et al. [42] for seven different individuals (with only a maximum of 2 macro-VOIs per vertebra of $8 \times 8 \times 8\,mm^3$).

Fig. 7 helps corroborate the hypothesis formulated by Fyhrie et al. [42], which states that vertebral cancellous bone has, at the macroscopic scale length, the same BS/TV to BV/TV relationship for all people (R^2 = 0.92). To do that, this figure represents our computed specific surface area data (S_v = BS/TV (mm^{-1})) versus their corresponding computed porosity data (ε = 1 - BV/TV). In this sense, this figure is similar to the previous one but allows the incorporation of experimental regression curves obtained by other authors from different species, bones and locations [43,44]. Despite the minor differences observed, it can be concluded that the agreement is relevant. For example, the regression curve (a modified 5th order polynomial based on [43]) obtained by Daish et al. [44] for bovine trabecular bone perfectly fits our isotropic foam data. On the other hand, the empirical 5th order polynomial regression proposed by Martin [43] for his entire set of human bone data, also fits our vertebra data adequately. Moreover, our entire set of data (porous foams and lumbar vertebra) can be adjusted correctly to the simplest equation proposed by Fyhrie et al. [42] (i.e. $S_v = A \cdot x \cdot (1 - x)$; with A = 15.69(± 0.78) and squared correlation coefficient of R^2 = 0.72556, very close to the better linear fit represented in Fig. 7, i.e. R^2 = 0.72151).

The analysis made with the current data allows us to conclude that, from a geometric point of view, a single human vertebra contains, at low scale (for a specific micro-VOI dimension), the same information of "specific surface area vs. porosity" – in other words, the same basic law – that can also be found in other human bones (for example, femoral mid-shaft) for different patients, even at different biological ages [45]. This is an important finding that, despite the efforts made and the controversies formulated by other authors [45,46], should be studied more thoroughly with other bone species and tissues (healthy and/or diseased). Thus, the use of a single healthy vertebra should not be seen as a shortcoming of the present study; quite the opposite. Due to its internal anisotropy, a healthy vertebra contains micro-VOIs able to reproduce, in the micro-scale, the different tendencies observed in the macro-scale by other authors working with many classified (species, gender, age, etc.) entire vertebras (see Fig. 7). For the sake of clarity, it should be remembered that the ten different micro-VOIs studied in the L3 vertebra were appropriately selected to cover the whole vertebral body and subsequently capture the average expected picture. The analysis of the specific histomorphometric features of each of the micro-VOIs allowed us to obtain, with only a single sample and within the existing limitations on the computation of larger VOIs, the same trends measured by other authors evaluating many macroscopic samples [32,35].

Fig. 8 was another way to reveal average microstructure differences between the samples studied. In this case, larger 3D macro VOIs than those selected in Figs. 2–6 were used. A macro-VOI of $30.2 \times 30.2 \times 30.2\,mm^3$ was chosen for the WF and the BF while a macro-VOI of $27 \times 27 \times 27\,mm^3$ was used in the case of the vertebra ESA. In this study, 5 equidistant 2D macro-VOIs were selected along each of the main x, y and z directions to perform particle tracking in order to compute the 3D average tortuosity of each sample. Fig. 8 shows, as an example, one of these computations carried out for 50 particles moving through the selected macro-VOI with an initial velocity of 1 cm/s [37] and an outlet pressure equal to zero. The top

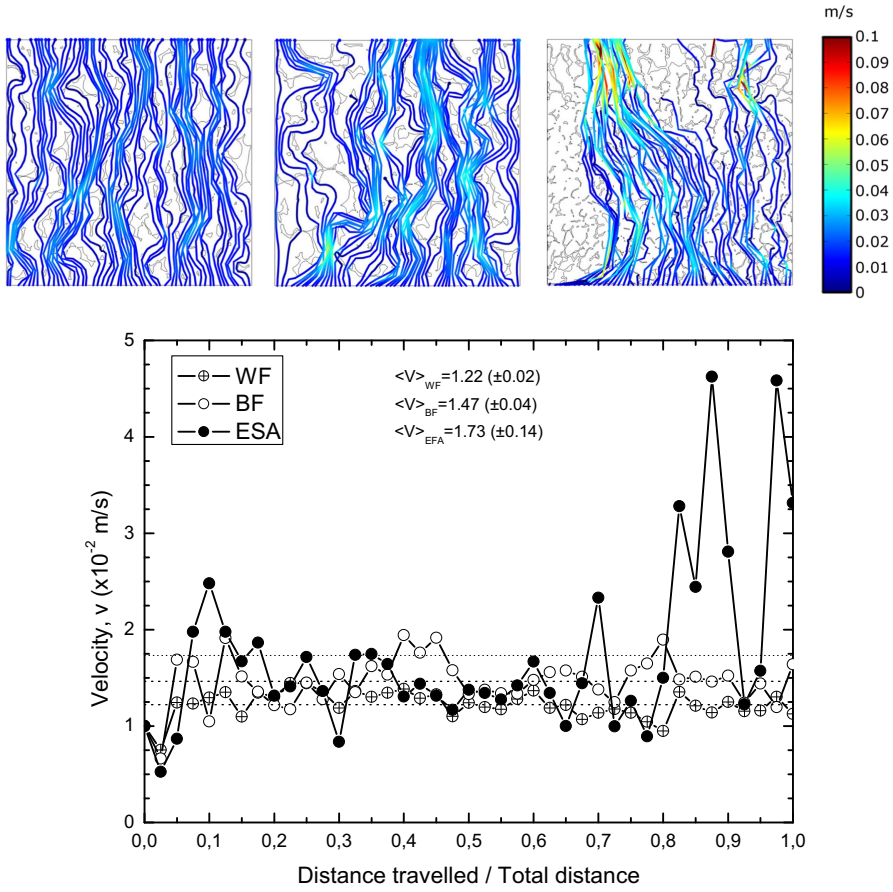

Fig. 8. Particle tracking computed in 2D for the samples studied (VOI = 30.2 × 30.2 mm^2) for WF and BF; VOI = (27 × 27 mm^2) for ESA; Number of particles = 50; Starting speed = 1 cm/s; Outlet pressure = 0). See the text for a detailed explanation.

pictures show the exact path followed by each particle through each sample (WF-left; BF-middle; ESA-right) together with their common colour velocity scale bar.

Basically, these pictures give an idea of the main flowing routes followed by particles. From this point of view, it can be concluded that, according to the total number of equivalent routes available for flowing, the samples follow in the macro-scale the order of WF ≥ BF > ESA. In other words, the vertebra presents a higher tendency for preferential flow in comparison with the foams. This agrees with the observations performed in Figs. 3–6 concerning the higher sensitivity of vertebra ESA when considering structure-related material properties at low scales. Particularly, this analysis provides insight into the role of vertebral anisotropy in relation to, for example, preferential flow of bone cement around fenestrated pedicle screws in clinical studies [47].

A more detailed analysis of the top pictures allowed to calculate the fraction of particles retained by the samples ($F_{PR} = P_R/N$), i.e. the number of particles retained (P_R; those that do not arrive at the end of the VOI) over the total number of particles moving through it (N = 50). Computations carried out in this case gave the following results: WF (F_{PR} = 2%), BF (F_{PR} = 8%), ESA (F_{PR} = 24%). Moreover, the average results computed along the x, y and z directions in the 5 selected equidistant 2D macro-VOIs (a total of 15 computations were carried out for each sample considering a number of 50 initial moving particles) gave similar values: WF (F_{PR} = 2.4(± 1.3)%), BF (F_{PR} = 2.8(± 1.2)%), and ESA (F_{PR} = 23(± 0.7)%).

Again, these results were in agreement with the average BV/TV values calculated for each macro-sample from the total number of micro-VOIs considered: WF (BV/TV(%) = 6.8(± 0.8)), BF (BV/TV (%) = 10.4(± 0.4)) and ESA (BV/TV(%) = 13.6(± 4.5)). This indicates that, under equal conditions, the more compact the sample the greater the number of particles retained. Obviously, this result is also related to another more significant histomorphometric index at low scale, i.e. Tb.Sp. In fact, calculations done to obtain this index gave the following results: WF (Tb.Sp(mm) = 1.17(± 0.04)), BF (Tb.Sp (mm) = 1.05(± 0.03)) and ESA (Tb.Sp(mm) = 0.97(± 0.04)); which are in agreement with the previous ones. This means that, under equal conditions, the lower the trabecular separation the greater the retention of particles.

In fact, this is also verified by looking at the colour scale bar of the top pictures, which clearly shows that, if individual particle speeds are considered, the samples are ordered, on average, from low (blue) to high (red) speed as follows: WF < BF < ESA. Again, this observation agrees with the expected behaviour of a fluid flow subjected to pressure gradient, i.e. the particles are accelerated when the channel through which they pass (Tb.Sp) decreases in size (see also the comments on Fig. 2).

Additionally, this effect is also captured in the bottom graph of Fig. 8, which shows the average speed evolution of all those particles that are entering the VOI at initial speed of 1 cm/s until they finally leave the macro-VOI, at boundary condition of null pressure (i.e. particles retained inside the macro-VOI are not considered). The average speed evolution is represented against the fraction of the total road travelled. This gives an idea of how an average particle moves through the microstructure of the macro-VOI while varying its average velocity according to the irregularities found in its way. The graph also shows the average velocity (< V >) of such average particle throughout its travel. The values obtained ($< V >_{WF}$(mm) = 1.22(± 0.02), $< V >_{BF}$(mm) = 1.47(± 0.04), $< V >_{ESA}$(mm) = 1.73(± 0.14)) agree again with the previous observations; i.e. the particles move faster if the channels through which they pass

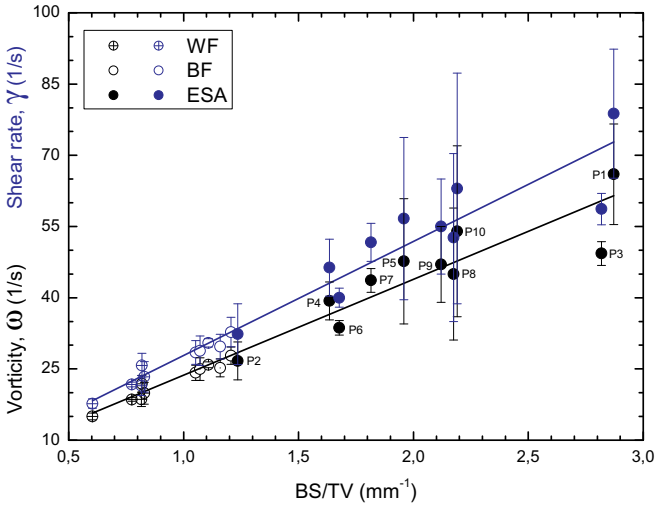

Fig. 9. Interdependence observed for the Vorticity (black) and the Shear rate (blue) as a function of the histomorphometric index BS/TV. A linear regression explained in both cases nearly 94% of the correlation. See the text for details. (For interpretation of the references to colour in this figure legend, the reader is referred to the web version of this article.)

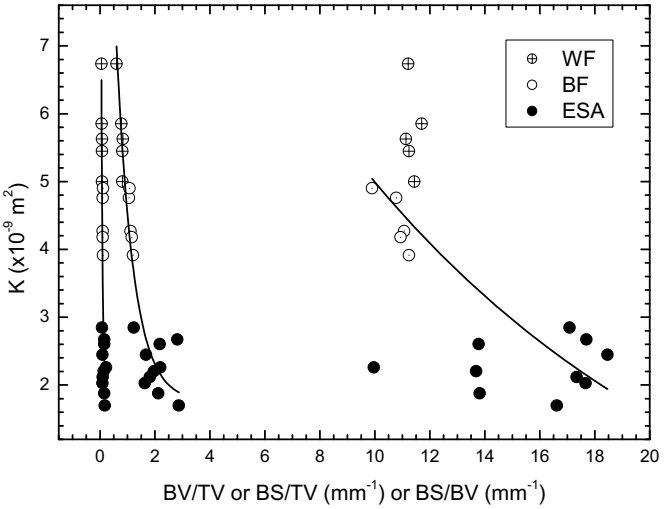

Fig. 10. Exponential decay correlation between the computed permeability of the samples and some important histomorphometric indices: BV/TV (left), BS/TV (middle) and BS/BV (right). The best correlation was obtained for the BS/TV index (93%). See the text for a detailed explanation.

diminish in size. Moreover, the computed data behind Fig. 8 allow us to calculate the tortuosity ($T = L_T/L_{VOI}$) of the samples, being L_T the average length travelled by all the particles that manage to reach the end of the macro-VOI and L_{VOI} the length or linear dimension of the macro-VOI. In this specific case, the results were: $T_{WF} = 1.08$; $T_{BF} = 1.12$; $T_{ESA} = 1.12$. Similar studies performed along the different x, y and z directions (15 computations for each sample) refined the above results as follows: $T_{WF} = 1.08(\pm 0.01)$; $T_{BF} = 1.10(\pm 0.02)$; $T_{ESA} = 1.13(\pm 0.02)$; which is consistent with the expected order of tortuosity (WF < BF < ESA).

Fig. 9 was an attempt to discover the best linear correlation between some computed intrinsic fluid properties (average shear rate, $\gamma(s^{-1})$; and average vorticity, $\omega(s^{-1})$) and some representative histomorphometric indices (BS/TV and BV/TV) of the porous microstructures (Fig. 9 only shows the best correlation obtained, which occurs for γ and ω versus BS/TV). This study was performed in the 3D micro-VOIs illustrated in Figs. 3–6 for each of the samples (WF, BF and ESA). A total of 3 computations (1 per axis) were done for each 3D micro-VOI in order to calculate the average values of γ and ω. The dynamic characteristics selected for the fluid were the ones of a Newtonian fluid in a laminar regime subjected to the boundary conditions shown in Fig. 1.f. It should be noted that these results were not aimed at providing concrete information about bone cement infiltration issues. Instead, they had the purpose to highlight the internal microstructural differences, computed under the same boundary conditions, between the different micro-VOIs and samples analysed.

Among the histomorphometric indices analysed, it was observed that the best correlation occurred for the BS/TV index; this is in fact the correlation shown in Fig. 9 ($\omega(1/s) = 3.5(\pm 2.1) + 20.2(\pm 1.3)\cdot(BS/TV)$; $R^2 = 0.93331$; and $\gamma(1/s) = 3.8(\pm 2.4) + 24.0(\pm 1.5)\cdot(BS/TV)$; $R^2 = 0.93552$). A similar representation (not shown), in which these fluid properties were plotted against the BV/TV index, gave worse correlations ($\omega(1/s) = 1.5(\pm 4.5) + 289.2(\pm 37.6)\cdot(BV/TV)$; $R^2 = 0.76638$; and $\gamma(1/s) = 1.9(\pm 5.5) + 340.5(\pm 46.1)\cdot(BV/TV)$; $R^2 = 0.75209$). The results clearly showed that the BS/TV index is the parameter that best captures the interdependence between the behaviour of the fluid and the internal micro architectural characteristics of the porous samples studied (i.e. the different micro-VOIs selected). Similar results were observed when the permeability of the samples was calculated with the same computation strategy as that followed to obtain Fig. 9; these results are shown in Fig. 10.

Fig. 10 represents the computed permeability data versus the computed histomorphometric indices BV/TV (left curve), BS/TV (middle curve) and BS/BV (right curve). The entire set of data was fitted to an exponential decay function ($y = y_0 + A_1 \cdot \exp(-x/t_1)$). The squared correlation coefficients indicated that the BS/TV index showed the best correlation ($R^2 = 0.92575$), followed by the BV/TV index ($R^2 = 0.59191$) and the derived BS/BV index ($R^2 = 0.4743$).

The conclusion seems to be the same as that drawn from Fig. 9. Thus, it is not the porosity (1-BV/TV) but the surface to total volume ratio (BS/TV) the index that best explains the difference of permeability between the studied foams and vertebra. This is not a minor fact since, traditionally, the porosity has been the main parameter to explain the variability of permeability in experimental studies evaluating populations of bone samples [12]. Despite this good correlation, the conclusion is not so clear when the analysis is restricted to each sample separately; the foams are isotropic and can be represented by a rod-like model (scalable model) while the real vertebra is anisotropic and must be represented by a mixed model composed of rods and plates (consequently, hardly scalable model). Linear regressions carried out in each sample separately showed exactly that. While the foams (WF and BF), in a joint evaluation, showed squared correlation coefficients for the permeability versus BV/TV and BS/TV of $R^2 = 0.81$ and $R^2 = 0.91$, respectively, the vertebra ESA showed no significant correlation at all ($R^2 = 0.08$ for BV/TV; $R^2 = 0.10$ for BS/TV). Other more classic fittings (not shown, based on Kozeny-Carman equation) showed no improvements.

A final conclusion can be obtained from Fig. 10. While our computed permeability data are very similar to those reported by other authors [9–14,26–28,31,43,44], our data do not clarify what structural indices properly explain the variability of permeability. Fortunately for us, this also agrees with literature [29,43,45,46]. In consequence, there is still much to do in the search for correlation between fluid-related properties of porous materials and their intrinsic histomorphometric features [48,49].

In the light of all the above, our results are enough to state that the commercial foams analysed (which are in fact isotropic) should not be used to simulate the infiltration behaviour of anisotropic structures like vertebral bone. Instead, with an exact internal knowledge of the bone microstructures [48,49], current technologies such as 3D [33] printing could be used to replicate at the macro-scale optimum biomimetic porous scaffolds to properly study, for example, in vitro bone cement infiltration issues.

4. Conclusion

The present research showed that commercial synthetic open-cell foams do not reproduce the anisotropic microstructure of healthy natural bone and, consequently, their suitability in studies assessing in vitro bone fluid infiltration is limited. The study also clarifies the discrepancies in the permeability obtained in the different micro-volumes-of-interest analysed. Our results suggest that, in order to achieve biomimetic scaffolds successfully mimicking human bone, it should be necessary to reproduce its intrinsic anisotropy at different length scales. In this sense, the extensive capabilities of current 3D printing technologies could play a relevant role. Moreover, the information obtained from micro-volumes-of-interests as those considered in this study could be scaled up to understand not only the macroscopic averaged isotropic and/or anisotropic behaviour of the samples studied, but also to improve the design of macroscopic porous implants better fitting particular histomorphometric conditions.

Declaration of competing interest

None.

Acknowledgements

The institutional support received through project 2017SGR253 is acknowledged (Agència de Gestió d'Ajuts Universitaris i de Recerca, Generalitat de Catalunya, Spain). This work received public funding through project DPI2016-77768-R (Ministerio de Economía y Competitividad, Spain). M.D. Vlad thanks research investigation financed by Grigore T. Popa University of Medicine and Pharmacy from Iasi, through project Contract-No. 29033/28.12.2016.

Data availability statement

Data will be made available on request.

References

[1] C.A. Inderjeeth, A.C. Foo, M.M. Lai, P. Glendenning, Efficacy and safety of pharmacological agent in managing osteoporosis in the old old: review of the evidence, Bone 44 (2009) 744–751, https://doi.org/10.1016/j.bone.2008.12.003.
[2] O. Johnell, Economic implication of osteoporotic spine disease: cost to society, Eur. Spine J. 12 (2003) S168–S169, https://doi.org/10.1007/s00586-003-0594-z.
[3] D. Felsenberg, A.J. Silman, M. Lunt, et al., Incidence of vertebral fracture in Europe: results from the European Prospective Osteoporosis Study (EPOS), J. Bone Miner. Res. 17 (2002) 716–724, https://doi.org/10.1359/jbmr.2002.17.4.716.
[4] J.C. Eck, S.D. Hodges, S.C. Humphreys, Vertebroplasty: a new treatment strategy for osteoporotic compression fractures, Am. J. Orthop. 31 (2002) 123–127.
[5] N.B. Watts, S.T. Harris, H.K. Genant, Treatment of painful osteoporotic vertebral compression fractures with percutaneous vertebroplasty or kyphoplasty, Osteoporos. Int. 12 (2001) 429–437, https://doi.org/10.1007/s001980170086.
[6] M.A.K. Liebschner, W.S. Rosenberg, T.M. Keaveny, Effects of bone cement volume and distribution on vertebral stiffness after vertebroplasty, Spine 26 (2001) 1547–1554, https://doi.org/10.1097/00007632-200107150-00009.
[7] M. Kayanja, K. Evans, R. Milks, I.H. Lieberman, The mechanics of polymethylmethacrylate augmentation, Clin. Orthop. Relat. Res. 443 (2006) 124–130, https://doi.org/10.1097/01.blo.0000200243.60426.57.
[8] Y.C. Hu, D.J. Hart, Complications of vertebroplasty and kyphoplasty, Techniques in Regional Anesthesia and Pain Management 11 (2007) 164–170, https://doi.org/10.1053/j.trap.2007.05.010.
[9] M.J. Grimm, J.L. Williams, Measurements of permeability in human calcaneal trabecular bone, J. Biomech. 30 (1997) 743–745, https://doi.org/10.1016/S0021-9290(97)00016-X.
[10] R.S. Ochia, R.P. Chin, Hydraulic resistance and permeability in human lumbar vertebral bodies, J. Biomech. Eng. 124 (2002) 533–537, https://doi.org/10.1115/1.1503793.
[11] G. Baroud, J.Z. Wu, M. Bohner, S. Sponagel, T. Steffen, How to determine the permeability for cement infiltration of osteoporotic cancellous bone, Med. Eng. Phys. 25 (2003) 283–288, https://doi.org/10.1016/S1350-4533(02)00223-0.
[12] G. Baroud, R. Falk, M. Crookshank, S. Sponagel, T. Steffen, Experimental and theoretical investigation of directional permeability of human vertebral cancellous bone for cement infiltration, J. Biomech. 37 (2004) 189–196, https://doi.org/10.1016/S0021-9290(03)00246-X.
[13] E.A. Nauman, K.E. Fong, T.M. Keaveny, Dependence of intertrabecular permeability on flow direction and anatomic site, Ann. Biomed. Eng. 27 (1999) 517–524, https://doi.org/10.1114/1.195.
[14] J.A. Szivek, M. Thomas, J.B. Benjamin, Characterization of a synthetic foam as a model for human cancellous bone, J. Appl. Biomater. 4 (1993) 269–272, https://doi.org/10.1002/jab.770040309.
[15] M.S. Thompson, I.D. McCarthy, L. Lidgren, Compressive and shear properties of commercially available polyurethane foams, J. Biomech. Eng. 125 (2003) 732–734, https://doi.org/10.1115/1.1614820.
[16] P.S.D. Patel, D.E.T. Shepherd, D.W.L. Hukins, Compressive properties of commercially available polyurethane foams as mechanical models for osteoporotic human cancellous bone, BMC Musculoskelet. Disord. 9 (2008) 137, https://doi.org/10.1186/1471-2474-9-137.
[17] A.E. Johnson, T.S. Keller, Mechanical properties of open-cell foam synthetic thoracic vertebrae, J. Mater. Sci. Mater. Med. 19 (2008) 1317–1323, https://doi.org/10.1007/s10856-007-3158-7.
[18] J.S. Thomsen, E. Ebbesen, L. Mosekilde, Zone-dependent changes in human vertebral trabecular bone: clinical implications, Bone 30 (2002) 664–669, https://doi.org/10.1016/S8756-3282(02)00686-5.
[19] L.J. Gibson, M.F. Ashby, Cellular Solids: Structure and Properties, (1988), https://doi.org/10.1017/CBO9781139878326.
[20] S. Gómez, M.D. Vlad, J. López, M. Navarro, E. Fernández, Characterization and three-dimensional reconstruction of synthetic bone model foams, Mater. Sci. Eng. C Mater. Biol. Appl. 33 (2013) 3329–3335, https://doi.org/10.1016/j.msec.2013.04.013.
[21] E.A. Moreira, J.R. Coury, The influence of structural parameters on the permeability of ceramic foams, Braz. J. Chem. Eng. 21 (2004) 23–33, https://doi.org/10.1590/S0104-66322004000100004.
[22] E.A. Moreira, M.D.M. Innocentini, J.R. Coury, Permeability of ceramic foams to compressible and incompressible flow, J. Eur. Ceram. Soc. 24 (2004) 3209–3218, https://doi.org/10.1016/j.jeurceramsoc.2003.11.014.
[23] A. Bhattacharya, V.V. Calmidi, R.L. Mahajan, Thermophysical properties of high porosity metals foams, Int. J. Heat Mass Transf. 45 (2002) 1017–1031, https://doi.org/10.1016/S0017-9310(01)00220-4.
[24] K.K. Bodla, J.Y. Murthy, S.V. Garimella, Microtomography-based simulation of transport through open-cell metal foams, Numerical Heat Transfer, Part A: Applications 58 (2010) 527–544, https://doi.org/10.1080/10407782.2010.511987.
[25] I. Ochoa, J.A. Sanz-Herrera, J.M. García-Aznar, M. Doblaré, D.M. Yunos, A.R. Boccaccini, Permeability evaluation of 45S5 Bioglass® –based scaffolds for bone tissue engineering, J. Biomech. 42 (2009) 257–260, https://doi.org/10.1016/j.jbiomech.2008.10.030.
[26] A. Syahrom, M.R. Abdul Kadir, J. Abdullah, A. Öchsner, Permeability studies of artificial and natural cancellous bone structures, Med. Eng. Phys. 35 (2013) 792–799, https://doi.org/10.1016/j.medengphy.2012.08.011.
[27] A. Syahrom, M.R. Abdul Kadir, M. Nor Harun, A. Öchsner, Permeability study of cancellous bone and its idealised structures, Med. Eng. Phys. 37 (2015) 77–86, https://doi.org/10.1016/j.medengphy.2014.11.001.
[28] J.C.M. Teo, S.H. Teo, Permeability study of vertebral cancellous bone using micro-computational fluid dynamics, Computer Methods in Biomechanics and Biomedical Engineering 15 (2012) 417–423, https://doi.org/10.1080/10255842.2010.539563.
[29] R.P. Widmer, S.J. Ferguson, On the interrelationship of permeability and structural parameters of vertebral trabecular bone: a parametric computational study, Computer Methods in Biomechanics and Biomedical Engineering 16 (2013) 908–922, https://doi.org/10.1080/10255842.2011.643787.
[30] A.J. Beaudoin, W.M. Mihalko, W.R. Krause, Finite element modelling of polymethylmethacrylate flow through cancellous bone, J. Biomech. 24 (1991) 127–136, https://doi.org/10.1016/0021-9290(91)90357-S.
[31] M.R. Dias, P.R. Fernandes, J.M. Guedes, S.J. Hollister, Permeability analysis of scaffolds for bone tissue engineering, J. Biomech. 45 (2012) 938–944, https://doi.org/10.1016/j.jbiomech.2012.01.019.
[32] Y. Chevalier, I. Santos, P.E. Müller, M.F. Pietschmann, Bone density and anisotropy affect periprosthetic cement and bone stresses after anatomical glenoid replacement: a micro finite element analysis, J. Biomech. 49 (2016) 1724–1733, https://doi.org/10.1016/j.jbiomech.2016.04.003.
[33] F. Baino, E. Fiume, J. Barberi, S. Kargozar, J. Marchi, J. Massera, E. Verné, Processing methods for making porous bioactive glass-based scaffolds – a state-of-the-art review, Int. J. Appl. Ceram. Technol. 16 (2019) 1762–1796, https://doi.org/10.1111/ijac.13195.
[34] P. Saparin, W. Gowing. Mid Term Report for ESA-Project: 2D and 3D Quantification of Bone Structure and Its Changes in Microgravity Condition by Measures of Complexity. Max Planck Institute of Colloids and Interfaces, Germany (MPI). (ESTEC Contract # 14592/00/NL/SH).
[35] M. Doube, M.M. Kłosowski, I. Arganda-Carreras, F. Cordeliéres, R.P. Dougherty, J. Jackson, B. Schmid, J.R. Hutchinson, S.J. Shefelbine, BoneJ: free and extensible bone image analysis in ImageJ, Bone 47 (2010) 1076–1079, https://doi.org/10.1016/j.bone.2010.08.023.
[36] C.A. Schneider, W.S. Rasband, K.W. Eliceiri, NIH Image to ImageJ: 25 years of image analysis, Nat. Methods 9 (2012) 671–675, https://doi.org/10.1038/nmeth.2089.
[37] S.G. González, M.D. Vlad, J.L. López, E.F. Aguado, Advantageous new conic cannula for spine cement injection, Spine 39 (2014) 1549–1557, https://doi.org/10.1097/BRS.0000000000000459.
[38] G. Lewis, Viscoelastic properties of injectable bone cements for orthopaedic applications: state-of-the-art review, J. Biomed. Mater. Res. Part B: Appl. Biomater. 98B (2011) 171–191, https://doi.org/10.1002/jbm.b.31835.
[39] C. Liu, Y. Huang, J. Chen, The physicochemical properties of the solidification of

calcium phosphate cement, J. Biomed. Mater. Res. Part B: Appl. Biomater. 69B (2004) 73–78, https://doi.org/10.1002/jbm.b.20032.
[40] R. Singh, P.D. Lee, Trevor C. Lindley, R.J. Dashwood, Emilie Ferrie, T. Imwinkelried, Characterization of the structure and permeability of titanium foams for spinal fusion devices, Acta Biomater. 5 (2009) 477–487, https://doi.org/10.1016/j.actbio.2008.06.014.
[41] J. Despois, A. Mortensen, Permeability of open-pore microcellular materials, Acta Mater. 53 (2005) 1381–1388, https://doi.org/10.1016/j.actamat.2004.11.031.
[42] D.P. Fyhrie, S.M. Lang, S.J. Hoshaw, M.B. Schaffler, R.F. Kuo, Human vertebral cancellous bone surface distribution, Bone 17 (1995) 287–291, https://doi.org/10.1016/8756-3282(95)00218-3.
[43] R.B. Martin, Porosity and specific surface of bone, Crit. Rev. Biomed. Eng. 10 (1984) 179–222.
[44] C. Daish, R. Blanchard, K. Gulati, D. Losic, D. Findlay, D.J.E. Harvie, P. Pivonka, Estimation of anisotropic permeability in trabecular bone based on microCT imaging and pore-scale fluid dynamics simulations, Bone Reports 6 (2017) 129–139, https://doi.org/10.1016/j.bonr.2016.12.002.
[45] C. Lerebours, C.D.L. Thomas, J.G. Clement, P.R. Buenzli, P. Pivonka, The relationship between porosity and specific surface in human cortical bone is subject specific, Bone 72 (2015) 109–117, https://doi.org/10.1016/j.bone.2014.11.016.
[46] N.L. Fazzalari, D.J. Crisp, B. Vernon-Roberts, Mathematical modelling of trabecular bone structure: the evaluation of analytical and quantified surface to volume relationships in the femoral head and iliac crest, J. Biomech. 22 (1989) 901–910, https://doi.org/10.1016/0021-9290(89)90074-2.
[47] S.G. González, G.C. Bastida, M.D. Vlad, J.L. López, P.B. Caballero, L.A. Galovich, M.R. Arguisjuela, E.F. Aguado, Analysis of bone cement distribution around fenestrated pedicle screws in low bone quality lumbosacral vertebrae, International Orthopaedics (SICOT) 43 (8) (2019) 1873–1882, https://doi.org/10.1007/s00264-018-4115-4.
[48] G.F. D'Urso Labate, F. Baino, M. Terzini, A. Audenino, C. Vitale-Brovarone, P. Segers, R. Quarto, G. Catafano, Bone structural similarity score: a multi-parametric tool to match properties of biomimetic bone substitutes with their target tissues, J. Appl. Biomater. Func. Mater. 14 (2016) e277–e289, https://doi.org/10.5301/jabfm.5000283.
[49] G.F. D'Urso Labate, G. Catafano, C. Vitale-Brovarone, F. Baino, Quantifying the micro-architectural similarity of bioceramic scaffolds to bone, Ceram. Int. 43 (2017) 9443–9450, https://doi.org/10.1016/j.ceramint.2017.04.121.